Black hole head-on collisions and gravitational waves with fixed mesh-refinement and dynamic singularity excision

Ulrich Sperhake,[1] Bernard Kelly,[1,2] Pablo Laguna,[1,3] Kenneth L. Smith,[1] and Erik Schnetter[4]

[1]*Center for Gravitational Wave Physics,*
Penn State University, University Park, PA 16802
[2]*Center for Gravitational Wave Astronomy,*
University of Texas at Brownsville, Brownsville, TX 78520
[3]*Institute for Gravitational Physics & Geometry*
Departments of Astronomy & Astrophysics and Physics
Penn State University, University Park, PA 16802
[4]*Max-Planck-Institut für Gravitationsphysik, Albert-Einstein-Institut, 14476 Golm, Germany*
(Dated: March 16, 2005)

We present long-term-stable and convergent evolutions of head-on black hole collisions and extraction of gravitational waves generated during the merger and subsequent ring-down. The new ingredients in this work are the use of fixed mesh-refinement and dynamical singularity excision techniques. We are able to carry out head-on collisions with large initial separations and demonstrate that our excision infrastructure is capable of accommodating the motion of the individual black holes across the computational domain as well as their their merger. We extract gravitational waves from these simulations using the Zerilli-Moncrief formalism and find the ring-down radiation to be, as expected, dominated by the $\ell = 2$, $m = 0$ quasi-normal mode. The total radiated energy is about 0.1 % of the total ADM mass of the system.

PACS numbers: 04.25Dm, 04.30Db

I. INTRODUCTION

One of the most urgent problems currently under investigation in general relativity is the coalescence of binary compact objects. The importance of this scenario largely arises from its significance for the new research field of gravitational wave astronomy; ground-based gravitational wave interferometric detectors, such as LIGO, GEO600, VIRGO and TAMA, have started collecting data. The in-spiral and merger of neutron stars and black holes is considered among the most promising sources of gravitational radiation to be detected by these instruments. Theoretical predictions of the resulting wave patterns will be important both for the detection and for the physical interpretation of such measurements. Although approximation techniques have been remarkably successful, the theoretical calculation of wave forms from compact object binaries will most likely require the numerical solution of the Einstein field equations.

Very important milestones have been achieved recently in the numerical modeling of compact object binaries. For instance, a few orbits of binary neutron stars are now possible (see e.g. [1, 2]). Also, with binary black holes, Brügmann et al. [3] have been able to carry out evolutions lasting for timescales longer than one orbital period. These varied efforts in modeling compact binary systems with numerical relativity share a common goal – to extract accurate waveform templates. This "Holy Grail" of numerical relativity, however, still eludes the community. A unique problem faced in the simulation of black hole spacetimes is the presence of physical singularities, which makes this task particularly delicate from a numerical point of view.

For a long time after the pioneering work of Eppley and Smarr in the 1970s [4, 5, 6], progress in numerical black hole evolutions was rather slow, and the codes suffered from instabilities after relatively short times. In contrast, the last few years have seen a change of strategy in the area of numerical relativity. More emphasis has been put on analyzing the structure of the evolution equations underlying the numerical codes (see e.g. [7, 8, 9, 10, 11, 12, 13, 14, 15, 16]). In combination with increased computational resources and advanced treatments of the spacetime singularities, this has led to vastly improved stability properties in the evolution of spacetimes with a single black hole either at rest or moving through the computational domain [17, 18, 19, 20]. In view of these encouraging results, attention has been shifting again toward the application of these techniques to the evolution and merger of binary black holes (see e.g. [3, 19, 21, 22, 23]).

In this paper, we will focus on the numerical evolution of head-on collisions of black holes implemented in the framework of dynamical singularity excision. The study of head-on colliding black holes has attracted a good deal of attention in the past, both numerically and analytically. We have already mentioned the early work of Eppley and Smarr who numerically evolved Misner data for equal-mass black hole collisions in axisymmetry. The waveforms extracted from these evolutions differ little in amplitude and phase from those obtained in perturbative calculations [6]. The head-on collision was re-investigated numerically in the 1990s [24, 25, 26, 27, 28] with generally good agreement between numerical results and those obtained from perturbation theory for various initial configurations. As a whole, the approximate analytic study

of binary black hole head-on collisions has been remarkably successful and has generated a wealth of literature. The late stage of the collision, when the separation of the two holes is sufficiently small, is well described by the *close limit* approximation (see e.g. [29, 30] as well as [31] for an estimate of the quality of the approximation using second-order perturbation theory). Similarly the particle approximation has been used to describe the in-fall phase with large black-hole separation either in the framework of post-Newtonian theory (see e.g. [32]) or using Newtonian trajectories with appropriate modifications [25, 26]. In particular, Anninos et al. [26] combined their "particle-membrane" technique with results from close limit calculations to provide estimates of the total radiated energy that are in good agreement with the results of numerical relativity over the whole range of initial black hole separations (see their Fig. 11).

The encouraging results of these perturbative approximations gave rise to the idea of combining them with full numerical evolutions via matching on slices of constant time. With this temporal matching, it was possible to extend the life of simulations of binary black holes which would otherwise stop because of numerical instabilities. This is now commonly known as the "Lazarus" approach; developed by Baker et al. [33] it has demonstrated good waveform agreement with non-linear evolutions.

The general picture that has emerged in analytic as well as numerical studies of equal mass head-on collisions is that gravitational wave emission is dominated by the $\ell = 2$, $m = 0$ quasi-normal oscillations of the post-merger black hole and that the total radiated wave energy is typically less than a percent of the system's ADM mass.

In spite of their limited astrophysical relevance, simulations of black hole head-on collisions still represent an important problem. In view of the eventual target, the in-spiral and merger of a binary black hole, these simulations constitute a key milestone in the development of numerical codes, a natural next step after successful evolutions of single black holes. While numerical codes have continued to improve in the simulation of head-on or grazing collisions [21, 34, 35], long-term-stable simulations have only been obtained rather recently by Alcubierre et al. [19] using the puncture method. In [22] the combination of this approach with the "Simple Excision" technique of Alcubierre and Brügmann [17] has been shown to preserve the long-term stability and yield good agreement in the wave forms. In this paper we present the first such long-term-stable evolutions obtained in fixed mesh-refinement as well as using the dynamical singularity excision technique.

The simulations presented in this paper have been obtained with the MAYA evolution code. This code and in particular its dynamical singularity excision technique are described in detail in [36] (referred to as Paper 1 from now on). A key development in recent months has been the combination of the MAYA code with the mesh-refinement package CARPET [37]. CARPET has enabled us to push the outer boundaries substantially further out

than was possible with the uni-grid version of MAYA; this was crucial in the extraction of gravitational wave signals.

The paper is organized as follows: The construction of binary black hole initial data used in this work is described in Sec. II, while the details of the numerical evolution scheme are given in Sec. III. The gravitational waveforms are analyzed in Sec. IV with regard to their convergence properties and the physical information they provide. We conclude in Sec. V with a discussion of our results and the implications for future work. In the appendix we present the details of the wave extraction using the Zerilli-Moncrief formalism on a single black hole background in Kerr-Schild coordinates. Throughout the paper, units are given in terms of M, with $M = {}^A m + {}^B m$, the sum of the bare masses of the individual black holes in the binary.

II. INITIAL DATA

The construction of astrophysically meaningful initial data for simulations of compact binaries is a highly non-trivial problem and represents an entire branch of research in numerical relativity (see [38] for a detailed overview).

For the simulations discussed in this work, we construct initial data according to the procedure of Matzner et al. [39], referred to from now on as "HuMaSh" data. This type of data has been used, for example, in binary grazing-collision evolutions by Brandt et al. [21]. The starting point of the HuMaSh data is the Kerr-Schild spacetime metric

$$g_{\mu\nu} = \eta_{\mu\nu} + 2 H l_\mu l_\nu \,, \qquad (1)$$

where $\eta_{\mu\nu}$ is the Minkowski metric, and l_μ is a null-vector with respect to both $g_{\mu\nu}$ and $\eta_{\mu\nu}$. In terms of 3+1 quantities, the Kerr-Schild metric is given by

$$\gamma_{ij} = \delta_{ij} + 2 H l_i l_j \,, \qquad (2)$$
$$\alpha = (1 + 2 H l^t l^t)^{-1/2} \,, \qquad (3)$$
$$\beta^i = -\frac{2 H l^t l^i}{1 + 2 H l^t l^t} \,. \qquad (4)$$

In particular, for a non-rotating black hole of mass m at rest at the origin

$$H = \frac{m}{r} \,, \qquad (5)$$
$$l_\mu = (1, \vec{l}) \,, \qquad (6)$$
$$\vec{l} = \frac{\vec{x}}{r} \,, \qquad (7)$$

with $r = \sqrt{\delta_{ij} x^i x^j}$.

As pointed out in Ref. [39], Kerr-Schild coordinates have two attractive features. First, with relevance to singularity excision, the coordinates penetrate the horizon. Second, the Kerr-Schild spacetime metric is form-

invariant under a boost transformation. Specifically, under a boost v along the z-axis, all that changes is

$$H = \frac{m}{R},$$
$$l_\mu = \left[\frac{\gamma(R - vZ)}{R}, \frac{x}{R}, \frac{y}{R}, \frac{\gamma(Z - vR)}{R} \right],$$

where $Z \equiv \gamma(z - vt)$ and $R^2 = x^2 + y^2 + Z^2$.

A spatial metric approximating initial data of two black holes, with bare masses ${}^A m$ and ${}^B m$ respectively, can be given by

$$\gamma_{ij} = {}^A\gamma_{ij} + {}^B\gamma_{ij} - \delta_{ij}, \tag{8}$$

where the ${}^A\gamma_{ij}$ and ${}^B\gamma_{ij}$ are to be understood as the Kerr-Schild spatial metric (2) evaluated at the corresponding black hole coordinate position and boost velocity. Following the HuMaSh prescription, the extrinsic curvature is constructed from

$$K^i{}_j = {}^A K^i{}_j + {}^B K^i{}_j, \tag{9}$$

where the ${}^A K^i{}_j$ and ${}^B K^i{}_j$ are also to be understood as the Kerr-Schild extrinsic curvature evaluated at the corresponding black hole coordinate position and boost velocity.

It is important to point out that the HuMaSh data do not provide a close limit; that is, as the coordinate separation of the black holes shrinks to zero, the resulting metric is not that of a single black hole with mass $M = {}^A m + {}^B m$. Furthermore, as given by (8) and (9), the HuMaSh data do not satisfy the Einstein constraints. As suggested by by Marronetti et al. [40], one could attenuate the constraint violations of the HuMaSh data using an exponential damping factor. Bonning et al. [41] used this attenuating procedure and provided a fairly detailed investigation of the general properties of the underlying HuMaSh data. In particular, they show that it has the correct gravitational binding energy in the Newtonian far-separation limit.

By construction the HuMaSh data will satisfy the constraint equations only in the limit of infinite separation of the two black holes. A rigorous treatment of a scenario with finite separation would thus require using the HuMaSh data as freely-specifiable background data and then solving the Hamiltonian and momentum constraint according to York's initial data prescription [42]. Since one of our primary goals is to extract gravitational waves from the black hole simulations, we need a sufficiently large computational domain, only attainable via mesh-refinement. Unfortunately, elliptic solvers operating on numerical grids with various refinement levels have not yet been developed in our Maya code. Using the uni-grid solvers available, on the other hand, is computationally prohibitive. Therefore, as with the grazing collision work in Ref. [21], the simulations in this paper were obtained using the constraint-violating HuMaSh initial data.

In this context one has to keep in mind that the constraints will always be violated at the level of numerical
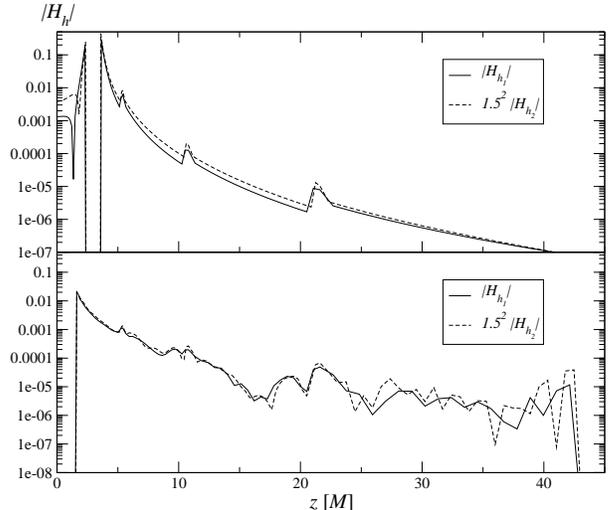

FIG. 1: Convergence analysis of the Hamiltonian constraint along the z-axis at $t = 0$ (upper panel) and $t = 25.92\,M$ (lower panel).

accuracy in a real simulation. In consequence, the constraint violations inherent to the HuMaSh construction are problematic only if they are significant relative to the limit set by finite grid resolutions in the course of the evolution. Furthermore, the constraint violations are reduced as we increase the initial separation of the black holes.

In order to estimate the significance of the constraint violations in the HuMaSh data relative to the numerical evolution errors, we have analyzed the convergence properties of the constraint violations in the course of the simulations. Because the initial data are not exactly constraint satisfying, we do not expect the values of the constraints to converge to zero at second order in the continuum limit. Let H_0 denote the Hamiltonian constraint violation at the continuum level inherent to the HuMaSh data. H_0 is thus independent of the grid resolution. For a second-order convergent evolution code, the numerical constraint violation H_h will be given by

$$H_h = H_0 + c\,h^2, \tag{10}$$

where h denotes the grid resolution and c is a function of space and time, independent of h. We have carried out two head-on collisions with black holes separated by a coordinate distance $6\,M$. These runs have resolutions $h_1 = 0.135\,M$ and $h_2 = h_1/1.5\,M$ on the finest refinement level respectively, with the grid spacing doubled in each of the three additional coarser levels. (These are the "coarse" and "medium" simulations in the convergence analysis of the waveforms in Sec. IV B.) For a second-order convergent code we expect the constraint violations
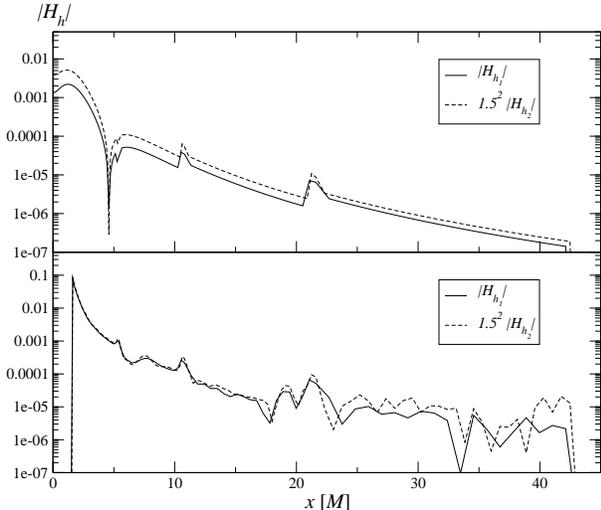
FIG. 2: Convergence analysis of the Hamiltonian constraint along the x-axis at $t = 0$ (upper panel) and $t = 25.92\,M$ (lower panel).

at the two resolutions to obey the relation

$$q \equiv \frac{H_{h_1}}{H_{h_2}} = \frac{H_0 + c\,h_1^2}{H_0 + c\,h_2^2}. \qquad (11)$$

It is instructive to consider the following two limiting cases of this equation. First, if the contribution H_0 due to the use of initially unsolved data dominates the total constraint violation, we obtain $q = 1$ and should observe no convergence at all. On the other hand, if H_0 is negligible, we expect second-order convergence and $q = 1.5^2$.

In view of this result, we have investigated the pointwise convergence of both the Hamiltonian and the momentum constraints. Fig. 1 shows the Hamiltonian constraint violation H_h along the z-axis (collision axis) for both runs, with the medium resolution result ($h_2 = h_1/1.5$) scaled by a factor of 1.5^2. The upper panel shows H_h at $t = 0$ and the lower panel at $t = 25.92\,M$. It is clear from this figure that at $t = 0$ second-order convergence is obtained in the strong field area close to the hole as well as in the far-field limit. At intermediate distances, on the other hand, the convergence deteriorates, in particular near $z = 0$, the region between the two holes. In the course of the evolution, however, the convergence approaches second order everywhere except in the domain of influence of the outer boundary, as clearly demonstrated in the lower panel of Fig. 1. The constraint violations are second-order convergent out to about $z = 22\,M$. We emphasize that these outer boundary effects are not related to the question of initial data and have also been observed, for example, in the puncture evolutions of Alcubierre et al. [22]. This viewpoint is further strengthened by the convergence analysis of the

waveforms in Sec. IV B which also reveal the propagation of noise from the outer boundaries as the limiting factor.

In order to shed more light on the constraint violations at small z, we show in Fig. 2 the Hamiltonian constraint violations along the x-axis at the same times. Due to the axisymmetry in the problem, the results along the y-axis are identical. Clearly the initial data do not exhibit second-order convergence, in agreement with the results of Fig. 1 near $z = 0$. In the course of the evolution, however, as the discretization error increases and dominates the total violations we do find second-order convergence of the Hamiltonian constraint except for the outer boundary effects mentioned above.

The results obtained for the momentum constraints show the same behavior, though they exhibit a stronger level of noise emanating from the refinement boundaries. We currently do not have an explanation for this discrepancy between Hamiltonian and momentum constraint but emphasize that the overall convergence of the momentum constraint is still close to second order up to the outer boundary effects.

In summary, our results confirm that the total constraint violation is indeed dominated by the numerical inaccuracies inevitably generated during time evolutions at currently available grid resolutions. This analysis generalizes the studies of Marronetti et al. [40] to include the discretization errors arising from the time evolution; these lead to an extension of the allowed range of grid spacings from their limiting value of $M/4$ to about $M/8$ as used in this work. While constraint solving of the initial data will be desirable for future simulations with higher resolutions, its effect on the overall constraint violations encountered in our simulations would be marginal at most. We emphasize in this context that this is only the case because of the absence of exponentially growing constraint violating modes in our simulations.

III. NUMERICAL EVOLUTION

From the operational point of view, it is convenient to divide a black hole head-on collision into pre-merger, merger and post-merger stages. In the pre-merger stage, the evolution contains two separate apparent horizons and therefore separate excision regions. The merger stage is signaled by the appearance of a single, highly distorted apparent horizon. Initially, these deformations of the horizon prevent the merger of the excision masks into a single spherical excision. The end of the merger stage is marked by the merger of excision masks when the deformations of the common apparent horizon have damped-out. The main constraint on the construction of the merged mask is that it must be completely inside the apparent horizon and fully contain the previous two disjoint excision regions. During the final stage (post-merger), the evolution consists of the settling or ringdown of the resulting black hole.

There are certain aspects besides the handling of the

excision region, such as gauge conditions, that require a different treatment during each of these stages. Before we discuss these differences in detail, we address those ingredients of the numerical evolution that remain unchanged throughout the complete simulation.

The specific implementation of the 3+1 BSSN formulation and the black hole excision technique used in the MAYA code have been described in detail in Paper 1. Here we provide a brief summary with particular regard to the changes necessary for working with fixed-mesh refinement.

We evolve the Einstein equations on a set of nested non-moving, uniform Cartesian grids with the resolution increasing by a factor of two for each additional refinement level. The Einstein field equations are evolved according to the BSSN 3+1 formulation [7, 11]. The exact shape of the equations as implemented in the code is given by Eqs. (6)-(10) in Paper 1; in particular this includes the additional term in the evolution of $\hat{\Gamma}^i$ introduced by Yo et al. [18] (the free parameter χ present in that term is set to 2/3 for all simulations discussed in this paper). These equations are evolved in time with the iterated Crank-Nicholson scheme. Spatial discretization is second-order centered finite differencing with the exception of advection derivatives contained in the Lie derivatives; these are approximated with one-sided second-order stencils. With regard to the treatment of refinement boundaries, we follow the recipe of Schnetter et al. [37] to avoid loss of convergence at these boundaries. For our code, this implies the use of a total of six buffer zones; two points (because of the one-sided derivatives mentioned above) for each of the three Crank-Nicholson iterations.

With the exception of gauge quantities specified algebraically as functions of the spacetime coordinates, we apply a Sommerfeld-like outgoing condition at the outer boundary [36]. At the excision boundary, we extrapolate all evolution fields from the computational interior using quadratic or, when populating previously excised points, cubic polynomials. With regard to mesh refinement we note that the black hole excision is actively implemented on the finest level, only migrating to the coarser levels via the restriction of grid functions; consequently, we always require that the black holes remain within the range of the finest grid. In practice this is not a limitation since it is precisely the black hole neighborhood where steep gradients are present and high resolution is therefore required.

In Paper 1, the uni-grid version of this code has been shown to produce long-term-stable evolutions of single Schwarzschild black holes as well as evolutions of moving black holes lasting for about $130\,M$. In [20] (referred to as Paper 2 from now on), we managed to extend the life times of these runs to at least $6000\,M$ by describing the slicing condition in terms of a densitized lapse function [cf. Eqs. (6)-(8) therein] and demonstrated second-order convergence of the code.

The remaining aspects of the numerical simulation are specific to the individual stages of the evolution and will now be discussed in turn. The main differences encountered here have to do with gauge and excision.

A. Pre-Merger Evolution

Pre-merger, our spacetime contains two apparent horizons. Within each apparent horizon, there is a curvature singularity, hidden from us by singularity excision. As the holes approach each other, the excised regions – or *excision masks* – are allowed to move also. The new locations of the excision masks must be found by somehow tracking the locations of the black hole singularities. One possibility is to track the singularities via an apparent horizon finder; we have found, however, that a simple Gaussian fit to the shape of the trace of the extrinsic curvature is equally effective for this purpose. As the excision regions move, grid points that were previously excised become part of the computational domain. These uncovered points must be supplied with valid data for all fields; this "re-population" of points is achieved through extrapolation onto the mask surface along coordinate normals to the surface. Both the Gaussian mask tracking and the re-population procedure have been treated in detail in Papers 1 and 2.

Besides the above, the current problem of evolving binary data raises new challenges. Primary among these is the question of gauge conditions. While substantial progress has been made in the recent past in deriving successful gauge conditions for evolutions that anchor black holes to a fixed coordinate location (see e.g. [3, 17, 18, 43, 44, 45, 46]) the question as to suitable gauge conditions for strongly time varying scenarios, such as spacetimes with moving black holes, remains largely unanswered.

In view of the successful simulations of single moving black holes in Paper 2, we have decided to pursue a similar approach for the binary system at hand, namely analytic shift and densitized lapse. A key benefit of using a densitized version of the lapse is that it facilitates an algebraic specification of the slicing condition, in terms of an analytic function of the spacetime coordinates, while preserving criteria for strong and symmetric hyperbolicity as derived in [47]. In contrast to the single black hole simulations of Paper 2, where algebraic forms of the shift and densitized lapse were available from the analytic single black hole solution, gauge conditions for our head-on collisions, in which the black holes exhibit changes in their coordinate location, require a suitable guess. We must emphasize that any gauge condition we introduce should not in principle affect the physical content in the spacetime. In practice, we specify gauge conditions that facilitate the merger and achieve long-term-stable evolutions.

We require that the lapse function and shift vector resemble those of a single, boosted Kerr-Schild black hole in the vicinity of each singularity, namely Eqs. (3) and

(4) respectively. Using these single, boosted black hole expressions, we construct the following gauge conditions:

$$\alpha = \left({}^A\alpha^{-2} + {}^B\alpha^{-2} - 1 \right)^{-\frac{1}{2}} \qquad (12)$$

$$\beta^i = \gamma^{ij} \left({}^A\beta_j + {}^B\beta_j \right) \qquad (13)$$

It is not difficult to show that (12) and (13) have a close limit. That is, at zero separation and boost velocity, they coincide with the lapse and shift of a single, non-rotating, non-boosted Kerr-Schild hole of mass $M = 2m$.

It is important to emphasize that the gauge conditions (12) and (13) require information about the coordinate location of the black hole singularities and boost velocities. Here, black hole coordinate location is not meant to be a formal statement about the precise location of the physical singularities, but it is merely used to represent the point with respect to which (12) and (13) are evaluated. Therefore, in order to use these gauge conditions, there remains the task of finding suitable trajectories for the black holes. We have found the following "Newtonian" trajectories adequate for this purpose:

$$\vec{r}(t) = \vec{r}_0 + \vec{v}_0 t + \frac{1}{2}\vec{a}_0 t^2 \,. \qquad (14)$$

Here $\vec{r}_0$ and $\vec{v}_0$ are the initial singularity position and boost velocity, respectively. The value for $\vec{a}_0$ is obtained iteratively using a small number of preliminary runs to ensure the largest gradients of the gauge fields remain well covered by the excision mask. During the evolution, the boost velocity needed to compute (12) and (13) is obtained simply from $\vec{v} = d\vec{r}/dt$.

B. The Merger of Excision Masks

The key point during the merger stage is, once a common apparent horizon has formed and been identified, to replace the individual spherical excision masks with a single spherical one. The size of this new excision region is determined by the minimum sphere containing the original excision masks. However, special care must be taken with regard to the timing of this replacement. One must check that the new spherical mask is fully contained within the apparent horizon. Typically, when the common horizon forms, it has an elongated or prolate shape. Therefore, a delay in merging the mask allows the common apparent horizon to become more spherical, thus facilitating the creation of a spherical merged mask. On the other hand, there is a constraint on how long this delay can be. Because of the extrapolations involved in the excision, one cannot delay the merger of the masks until their surfaces touch each other. Even if the common apparent horizon is not completely spherical, the masks are merged if there are not enough grid-points between the individual masks to carry out excision extrapolations. Of course, in this case one still has to continue to satisfy the requirement that the merged mask is contained within the apparent horizon. For the head-on collisions under consideration, we find that the common apparent horizon becomes almost spherical before the separation of individual masks decreases to the point of preventing excision extrapolations.

Resolution also plays a factor during the mask merger. If the grid resolution in the vicinity of the black holes is too coarse, the minimum coordinate separation of the individual masks required by excision extrapolations will be too large. In consequence, it becomes more difficult to find a spherical merged mask that comfortably fits within the common apparent horizon. For the typical resolution used in our simulations, $h = 0.135\,M$, two single-hole masks of radius $0.405\,M$ require a merged mask with radius of $1.1475\,M$. That is, single-hole masks with $40.5\,\%$ of the single-hole horizon radius mean the new excision radius is approximately $57\,\%$ of the common horizon radius.

C. Post-Merger Ring-Down

After the excision mask merger, the key change concerns the gauge conditions. Post-merger, the spacetime effectively represents a single ringing black hole, and the problem at hand is similar to that of evolving a single stationary hole. In Papers 1 and 2, we have demonstrated how this scenario can be simulated with long-term stability using either live gauge conditions or algebraic gauge using a densitized lapse. The same options apply to the post-merger stage of a black hole collision, and we have found that either approach provides long-term stability. For the extraction of wave forms, we find a similar situation: live and densitized algebraic gauge conditions generate waveforms that differ only within numerical errors. For simplicity, we use densitized algebraic gauge conditions (see Paper 1 and 2 for details).

There remains the question of how the transition from the superposed gauge (12) and (13) to a single black hole gauge takes place. As mentioned before, the gauge conditions (12) and (13) have the correct close limit (i.e. vanishing separation and boost velocities). Starting at the time when the masks are merged, we match the current "black hole positions" given by (14) to decelerating trajectories given by sixth-order polynomials in time. These new trajectory functions are such that the coordinate separation and boost velocities vanish within a time interval (typically $10\,M$). The order of the polynomial is fixed by requiring continuity of the boost velocity and acceleration.

IV. RESULTS

The spacetime of head-on collisions of non-spinning black holes is by construction axisymmetric. In the equal-mass case there is a further reflection symmetry across the plane perpendicular to the collision axis halfway between the holes. Although the simulations in

TABLE I: Setup parameters for the runs. D and L are the coordinate and proper initial separations. v_0 is the boost velocity and a_0 the "acceleration" parameter to compute the gauge trajectories.

Run	$D\,[M]$	$L\,[M]$	v_0	$a_0\,[M^{-1}]$
$D06$	6	5.49	0.289	0.040
$D10$	10	10.06	0.270	0.014

TABLE II: Grid parameters of the refinement levels used in the simulations. The number of grid points N includes ghost, symmetry and outer boundary zones. $r_{\max}$ is the extent in the x, y and z-directions.

ref-level	$h\,[M]$	N	$r_{\max}\,[M]$
1	0.135	67^3	8.505
2	0.27	67^3	17.01
3	0.54	67^3	34.02
4	1.08	134^3	140.4

this work are intrinsically 3D, we take advantage of these symmetries and evolve only one octant of the numerical domain. One of the primary goals of our work is to perform 3D-simulations of head-on collisions with initial separations never tried before. However, determining what constitutes a large separation has the following complication. Previous work on head-on collisions has used exclusively Misner or Brill-Lindquist initial data, as for example the recent long-term-stable simulations of Alcubierre et al. [19, 22]. To our knowledge, the only evolutions of binary Kerr-Schild (HuMaSh) data is the grazing collision of Brandt et al. [21], where the black holes had an initial coordinate separation of $5\,M$.

We must emphasize that there exists no unambiguous definition of a black hole separation; also, given that we are using HuMaSh initial data, direct comparison of our initial black hole coordinate separations with those from Misner or Brill-Lindquist initial data is not correct. An operational measure of higher physical significance is given by the horizon-to-horizon proper separation. That is, the proper 3D distance horizon-to-horizon computed along the collision axis within the hypersurface where the initial data resides. One should bear in mind that this proper separation is slicing-dependent. Additionally, our proper distance separation suffers from the effects due to constraint violations intrinsic to the HuMaSh data.

Table I gives the black hole coordinate (D) and proper (L) separations for the two sets of runs (labeled $D06$ and $D10$) performed in this work. In addition, the table gives the initial boost velocity (v_0) as well as the "acceleration" parameter (a_0) used to compute the trajectories required to construct the gauge variables [cf. Eq. (14)]. As a reference, the "Cook-Baumgarte" ISCO [48, 49] corresponds to a proper separation between 4.8 and $4.88\,M$. Similarly, the orbit simulation by Brügmann et al. [3] started from a proper separation of about $9\,M$.

We evolve the initial data on a set of four nested refinement levels, with resolution and extent as given in Table II. Except for the outermost level, grid spacing and extent always increase by a factor of two. We have found that a grid spacing significantly larger than $1.08\,M$ in the outer regions gives rise to substantial reflections of gravitational waves at the refinement boundary. For this reason we have pushed the outermost level to $140.4\,M$ without adding a further coarser level.

Using the setup described above, we obtain long-term-stable evolutions. The three simulation stages described in Sec. III are illustrated in Fig. 3. This figure contains
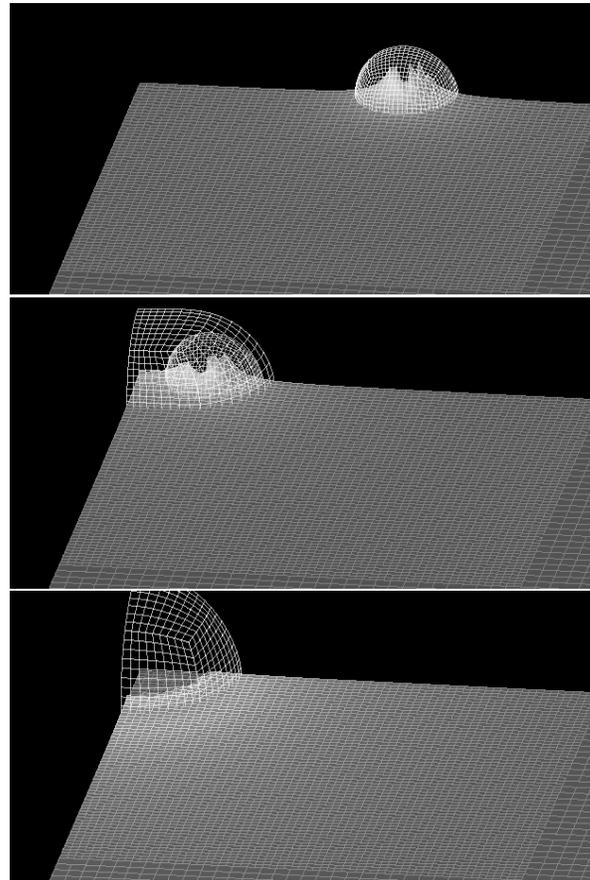

FIG. 3: Snapshots of the $D10$ run taken at times $t = 0$, 10.8 and $14\,M$. From top to bottom the panels show the individual holes with distinct apparent horizons (only one hole is visible due to the octant symmetry), a common apparent horizon forming around the individual trapped surfaces and a single apparent horizon surrounding a single excision region.

snapshots of the $D10$ run at times $t = 0$, $10.8\,M$ and $14\,M$, including the marginally trapped surfaces as calculated by Thornburg's AHFINDERDIRECT code [50, 51]. The upper panel shows the initial configuration with holes present at $z = \pm 5\,M$. As mentioned above the computational domain only includes the hole at $5\,M$ due to symmetry. During this pre-merger stage each hole is surrounded by its own apparent horizon (AH). In the middle
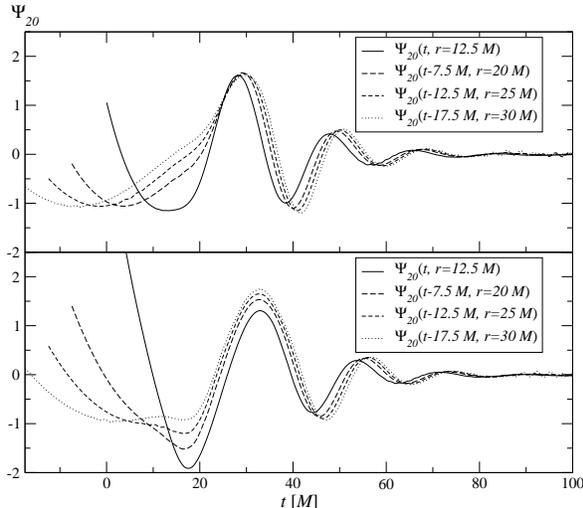
FIG. 4: The $\ell = 2, m = 0$ Zerilli function extracted at different radii for the $D06$ (upper panel) and $D10$ (lower panel) runs. The curves have been shifted in time by the difference in propagation time of the wave signal between the different radii.

FIG. 5: The $\ell = 2$, $m = 0$ component of the real part of the Newman-Penrose scalar ψ_4 extracted at different radii for the $D06$ (upper panel) and $D10$ (lower panel) runs. The curves have been shifted in time by the difference in propagation time of the wave signal between the different radii.

panel, the holes are sufficiently close to one another that a common AH has formed. However, as mentioned before, it is not possible yet to switch to a single excision region because of the elongated shape of the common apparent horizon. The lower panel shows the beginning of the post-merger stage.

A. Waveforms

We extract waveforms at radii 12.5, 20, 25 and $30\,M$ using the Zerilli-Moncrief formalism; details are given in App. A. In principle, it is desirable to extract gravitational waves at large radii so as to ensure that the assumptions inherent to the Zerilli-Moncrief extraction are satisfied. We observe two problems, however, which arise out of choosing excessively large radii. First, outer boundary effects require less time to propagate inward and reach the extraction radius. Second, the actual wave signal contained in the metric and curvature variables is weaker at larger radii and thus requires higher accuracy in the numerical evolution. In combination with the increasingly coarse resolution used in outer levels, this gives rise to a degree of distortion and noise in the extracted Zerilli function which is not present at smaller radii. We find the values used above to be a reasonable compromise for the post-merger stage of the head-on collision. In Fig. 4 we show the resulting $\ell = 2, m = 0$ waveforms, each shifted in time by the amount required by the signal to travel from $r = 12.5\,M$ to the corresponding extraction radius. All curves in the figure show a significant initial
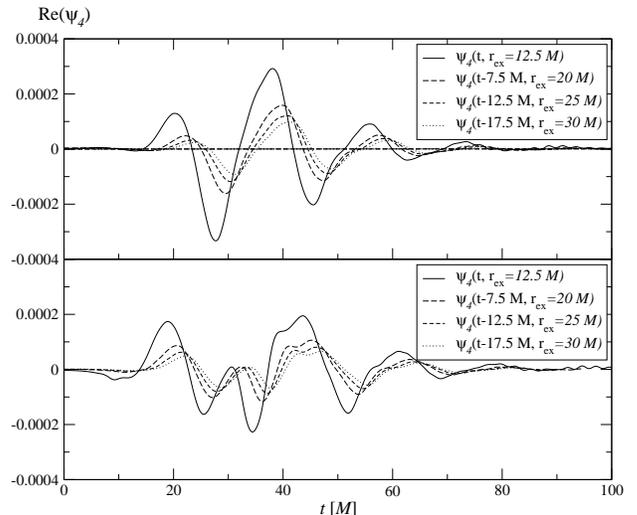
signal up to about $t \approx 10\,M$. We trace the origin of this signal to the fact that the two black holes are far apart in the early stages of the simulation and thus the assumption underlying the wave extraction technique, namely that the spacetime is that of a single black hole plus a perturbation, is not satisfied with sufficient accuracy during the pre-merger phase. This viewpoint is strengthened by the observation that the spurious signal is stronger for the larger black hole separation of case $D10$ in the lower panel of the figure. We further note in this context that the merger of the black holes occurs at $t = 5.4\,M$ and $11.75\,M$ respectively for cases $D06$ and $D10$. It is at about these times that the shifted waveforms extracted at different radii start showing better agreement with each other in the figures, while the spurious signal present at earlier times converges away at larger extraction radii.

Because the Zerilli potential becomes zero in the limit of infinite extraction radii, one would expect the curves in the individual panels of Fig. 4 to overlap exactly in this limit. The figure shows that this criterion is satisfied with increasing accuracy at larger radii. Still there remain small effects of back-scattering of the wave signal at the finite radii used in the extraction. The figure also reveals some noise developing at late times at larger radii; an analysis of the timing of the noise demonstrates that these are boundary effects propagating inward. Below, we will see that these effects limit the convergence properties of our code and thus the reliability of the results after the onset of noise in the waveforms.

An alternative to the Zerilli-Moncrief approach to wave extraction is provided by the Newman-Penrose formal-

ism; the Newman-Penrose Weyl scalar ψ_4 represents a measure of the outgoing gravitational wave content. We calculate this scalar via the "electric-magnetic" decomposition of the Weyl tensor as described in [52]. We use a null tetrad formed from an orthonormalized spherical coordinate tetrad, as an approximation to the more appropriate Kinnersley tetrad [53]. Because the $\ell = 2$, $m = 0$ quadrupole moment is the dominant contribution we show in Fig. 5 only this multipole of the real part of ψ_4 extracted at the same radii as the Zerilli function (the imaginary part of ψ_4 vanishes due to symmetry). As is obvious from a comparison of the two figures, we find the Newman-Penrose scalar to be more susceptible to numerical inaccuracies than the Zerilli function, especially for larger initial separations of the holes. While the upper panel of Fig. 5 qualitatively agrees with the Zerilli function in Fig. 4, the lower panel obtained for $D = 10\,M$ shows a significant deviation from the quasi-normal ringing exhibited by the Zerilli function. Note, however, that for both initial separations we do not observe in the Newman-Penrose scalar the spurious wave-signal at early stages of the evolution. This supports the view that this feature merely arises because the underlying assumptions of the Zerilli-extraction technique are not satisfied at early stages.

We believe the higher degree of noise and distortion in the Newman-Penrose scalars to be an artifact of the higher order of derivatives needed in their calculation, combined with the fact that their derivatives are calculated *before* integration over the coordinate sphere. Due to these difficulties, we will from now on restrict our analysis to the waveforms of Fig. 4 obtained with the Zerilli-Moncrief formalism. In order to estimate the quality of the waveforms, next we investigate their convergence properties.

B. Convergence

The discretization of the BSSN-evolution equations in the Maya code is implemented with second-order accuracy in the grid spacing h. The wave extraction, as described in Appendix A, involves numerical approximations of higher-order accuracy, such as the interpolation of grid functions onto the sphere of extraction and the evaluation of the integrals over the spheres. The numerical error in the wave functions should therefore be dominated by the second-order accuracy of the evolution of the field equations, and we expect the wave forms to exhibit second-order convergence.

In order to verify this numerically, we focus our attention on the head-on collision case $D06$ and carry out two additional runs. Compared with the resolutions listed in Table II, the two additional runs are finer by factors of $1/1.5$ and $1/1.5^2$. On the finest grid for each of the three runs, this leads to resolutions $h_1 = 0.135\,M$, $h_2 = 0.09\,M$ and $h_3 = 0.06\,M$, respectively. Because the coarsest mesh in $D06$ has an extent of $140.2\,M$, im-
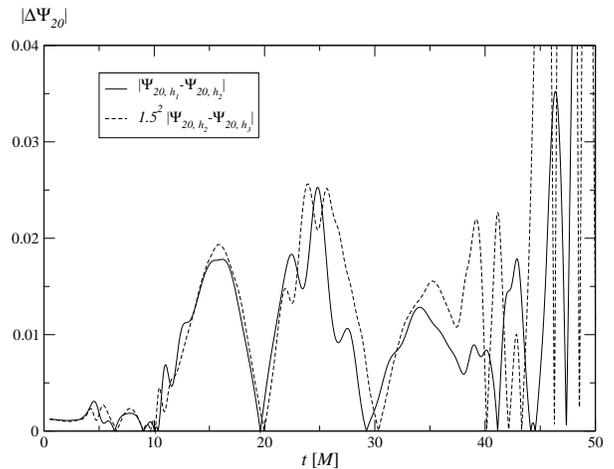

FIG. 6: Three-level convergence analysis for the $\ell = 2$, $m = 0$ Zerilli function extracted at $r = 7.5\,M$.

plementing the $1/1.5$ and $1/1.5^2$ refinements far exceeds the available memory of our hardware resources. For this reason, instead of using mesh-refinements with the sizes given in Table II, we have performed the convergence analysis using for each run four refinement levels of extent $r_{\max} = 5.4,\ 10.8,\ 21.6$ and $43.2\,M$. The key difference compared with the simulations discussed above is that outer boundary effects will reach the extraction radii at earlier times. To mitigate this effect we extract the Zerilli function at the smaller radius $r_{\mathrm{ex}} = 7.5\,M$ for this analysis.

In Fig. 6 we show the difference in the $\ell = 2$, $m = 0$ Zerilli function obtained for the three different resolutions. The difference in Ψ_{20} between the medium and high resolution runs has been amplified by the factor 1.5^2 expected for second-order convergence. The resulting curve agrees reasonably well with the difference obtained from using the low and medium resolution until about $35\,M$, indicating second-order convergence. After that time, noise originating from the outer boundary at $43.2\,M$ has reached the extraction radius at $7.5\,M$ and spoils the convergence properties. This result is confirmed by analysis at larger radii where second-order convergence is observed for correspondingly shorter periods of time. We conclude that our code facilitates second-order convergent wave extraction until outer boundary effects have had the time to propagate inward toward the radius of wave extraction. For the simulations presented in the previous subsection, this result implies reliable waveforms up to a time of about $100 - 125\,M$ depending on the extraction radius. While outer boundary effects clearly affect the accuracy of our simulations, we emphasize that we have not observed any sign of instabilities: all simulations presented in this work have continued for many hundreds or

TABLE III: Quasi-normal ringing damping σ and oscillation frequency ω measured from the extracted waveforms. The final column gives the percentage of the initial ADM mass radiated away in the form of gravitational waves as derived from Eq. 16

run	r_{ex}/M	σM_{ADM}	ωM_{ADM}	E_{rad} [%]
$D06$	12.5	0.0917	0.365	0.20
$D06$	20	0.0921	0.362	0.15
$D06$	25	0.0923	0.363	0.14
$D06$	30	0.0947	0.366	0.14
$D10$	12.5	0.0973	0.369	0.37
$D10$	20	0.0963	0.363	0.16
$D10$	25	0.0960	0.365	0.14
$D10$	30	0.0976	0.366	0.13

FIG. 8: The apparent horizon mass as a function of time calculated for the $D06$ (upper panel) and $D10$ (lower panel) simulation.
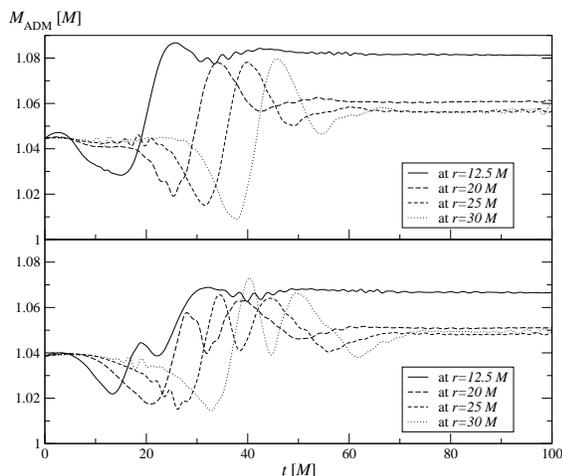

FIG. 7: ADM mass as a function of time evaluated at various radii for the $D06$ (upper panel) and $D10$ (lower panel) simulation.

even thousands of M gradually approaching a stationary spacetime containing a single black hole.

C. Quasi-normal Ringing, Masses and Radiated Energy

Previous studies have shown that most of the gravitational radiation of a head-on collision is emitted in the post-merger ring-down phase, with the total radiated energy typically being less than a percent of the total initial mass [24, 26, 29, 30]. Furthermore, the quasi-normal ringing of the post-merger black hole is dominated by the $\ell = 2$, $m = 0$ mode with small contributions from the $\ell = 4$, $m = 0$ multipole. Our simulations represent the first head-on collisions with wave extraction using Kerr-Schild type data. They are in good agreement with
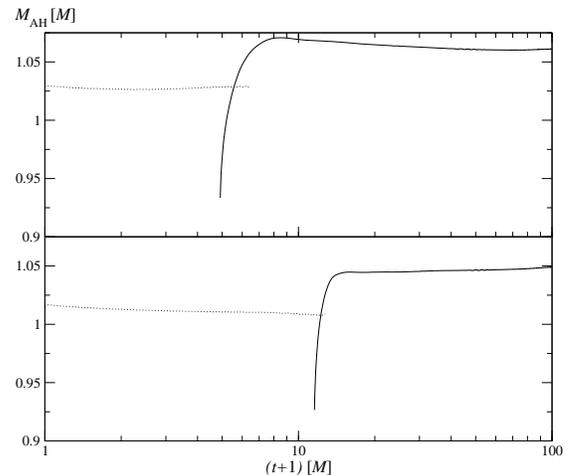
the picture described above.

We first note that up to $\ell = 3$ the only multipole with a notable wave signal is the $\ell = 2$, $m = 0$ quadrupole shown in Fig. 4. Second, we have performed least-square fits of the waveforms to

$$f(t) = A\, e^{-\sigma t} \cos \omega t. \tag{15}$$

in order to calculate the ringing damping σ and oscillation frequency ω. The results are given in Table III. The resulting damping and oscillation frequency values agree within about 10 %. For comparison, the quasi-normal mode spectrum of the Schwarzschild black hole calculated by Chandrasekhar and Detweiler [54] predicts $\sigma\mathcal{M} = 0.0890$, $\omega\mathcal{M} = 0.374$, where $\mathcal{M}$ denotes the mass associated with the black hole background spacetime. In Table III, the results are reported in units of the total initial ADM mass M_{ADM}. The differences between these two masses are the radiated energy and numerical errors.

In the course of the evolution we numerically approximate the ADM mass by evaluating the ADM integral at finite extraction radii. The result is shown in Fig. 7 for simulation $D06$ in the upper panel and $D10$ in the lower panel. The initial values agree well with the sum γM of the special relativistic masses of the two individual holes moving with the velocities given in Table I, that is $M_{\mathrm{ADM}} = 1.045\, M$ and $1.039\, M$ respectively. During the evolution the numerical ADM mass remains within a few percent of the initial value but in contrast to intuitive expectations it increases slightly rather than decreases after the gravitational waves have passed the extraction radius. Even though this increase becomes less pronounced at larger extraction radii we do not consider this calculation of the ADM mass sufficiently accurate to support a calculation of the total radiated gravitational

wave energy from conservation arguments.

In Fig. 8, we plot the apparent horizon masses as calculated by AHFINDERDIRECT for the two cases $D06$ (upper) and $D10$ (lower panel). During the pre-merger stage there is no common apparent horizon present and we plot instead the sum of the horizon masses associated with the individual holes (dotted curves). In contrast the solid curve represents the horizon mass of the single post-merger hole. In the early stages after merger the horizon mass shows a significant increase in time but quickly settles down in the final values of $1.06\,M$ and $1.05\,M$ respectively. These values show good agreement with the values $1.045\,M$ and $1.039\,M$ used for the black hole background mass for the wave extraction. Theoretically one would not expect the horizon mass to decrease as a function of time. We attribute the decrease by about one percent visible after the merger in the upper panel of Fig. 8 to numerical inaccuracies.

We estimate the total radiated energy from the Landau-Lifshitz formula (see e. g. [55]) which gives the radiated power as

$$\mathrm{P} = \frac{1}{96\pi}\Psi_{,\mathrm{t}}^2,\qquad(16)$$

where the constant factor arises from our definition of the Zerilli function in Eq. (A5). Ideally this function needs to be evaluated at null infinity. As this is not possible in this type of computation, we approximate the exact result by calculating the radiated energy at various finite radii. For this purpose, we have evaluated the integral of P from $t = 0$ to $t = 140\,M - r_{\mathrm{ex}}$; that is, we have excluded late times when the extraction radius is causally connected to the outer boundary. The results are shown in the last column of Table III and show the impact at small extraction radii of the spurious signal in the Zerilli function at early times when the two holes are still far apart from each other. This feature leads to an overestimate of the radiated energy but quickly converges away if we extract at larger radii. A close investigation reveals that this spurious contribution drops to a few percent of the total radiated energy at $r_{\mathrm{ex}} = 30\,M$ in the case $D10$ and even less in the case $D06$. Within these error bounds we thus find a radiated energy of about 0.14 and 0.13 percent of the total ADM mass of the system.

V. CONCLUSIONS

We have presented the first long-term-stable binary black hole collisions with wave extraction using fixed mesh-refinement, Kerr-Schild type initial data and dynamical excision. While the success of our dynamical excision technique has been demonstrated in the past in the case of static and dynamic single black hole spacetimes, the results in the present work demonstrate the applicability of our dynamical excision to binary black hole systems with gravitational wave generation.

Our simulations start from initial data constructed via superposition of two single Kerr-Schild black holes, namely HuMaSh data. We have demonstrated by convergence analysis of the Hamiltonian and momentum constraints that the inherent constraint violations in the HuMaSh data is not significant compared with the level of accuracy allowed by current computational resources.

We have conceptually divided the evolutions into three stages: the initial in-fall, the merger and the post-merger ring-down of the resulting single black hole. In particular during the first two stages, special care must be taken to ensure that the excision region always be entirely contained inside the apparent horizon. For this purpose, we have calculated the apparent horizon at each time step and verified that no causal violation of the excision technique occurs.

We have extracted gravitational waves using the Zerilli-Moncrief approach applied to a black hole background spacetime in Kerr-Schild coordinates. Our results confirm previous findings. Wave emission is dominated by the quasi-normal ringing of the single post-merger black hole. Up to $\ell = 3$ the only notable contribution is the $\ell = 2$, $m = 0$ quadrupole. Comparison of the damping and oscillation frequencies with analytic results shows good agreement. We do not find the accuracy in calculating the ADM or the apparent horizon mass sufficient, however, to support a calculation of the total radiated gravitational wave energy purely from conservation principles. Instead, we use the Landau-Lifshitz formula to calculate the radiated energy from the Zerilli function. We find this energy to be of the order of 0.1 % of the ADM mass. Our results demonstrate the need to extract gravitational radiation at sufficiently large radii in order to facilitate reasonable accuracy. In particular, we observe a spurious wave signal in the Zerilli function caused by a systematic deviation during the early pre-merger stage of the numerical spacetime from a perturbed single black hole spacetime. The wave contribution due to this spurious feature converges away as the extraction is carried out at larger radii.

We have also calculated the Newman-Penrose scalar ψ_4 as an alternative measure of the emitted gravitational radiation. While the results qualitatively confirm those obtained using the Zerilli approach, at least for smaller initial black hole separations, we find the Newman-Penrose scalars to be significantly more vulnerable to the development of numerical noise. In future work we plan to investigate how a more accurate calculation of these scalars can be achieved inside our code.

APPENDIX A: WAVE EXTRACTION USING THE ZERILLI-MONCRIEF FORMALISM

Our extraction of gravitational waves is based on the gauge invariant perturbation formalism of Moncrief [56]. A more detailed description of how this facilitates the extraction of gravitational waves from numerical simulations is given in [57]. Applications of this method can be found, for example, in [26] or [58].

The key idea is that at sufficiently large distance from a strong field source, the spacetime metric $g_{\mu\nu}$ can be viewed as a spherically symmetric background plus non-spherical perturbations which obey the Regge-Wheeler

equation (odd) and the Zerilli equation (even parity perturbations) respectively. In our case the background will be given by that of a single, non-rotating black hole in Kerr-Schild coordinates. Strictly speaking, the coordinates are ingoing-Eddington-Finkelstein coordinates, namely Kerr-Schild coordinates in the case of a non-rotating black hole. The symmetry properties of an equal mass head-on collision imply that the odd perturbations vanish, so we will restrict our attention to the even parity case.

Given the Kerr-Schild background metric

$$g_{\mu\nu}^{\rm B} dx^\mu dx^\nu = -\left(1 - \frac{2\mathcal{M}}{r}\right) dt^2 + \frac{4\mathcal{M}}{r} dt\, dr$$
$$+ \left(1 + \frac{2\mathcal{M}}{r}\right) dr^2 + r^2 d\Omega, \quad (A1)$$

the first-order metric perturbations, expanded in Regge-Wheeler tensor harmonics [59], can be written as

$$h_{\mu\nu} = \sum_{\ell m} h_{\mu\nu}^{\ell m}, \quad (A2)$$

where

$$h_{\mu\nu}^{\ell m} = \begin{pmatrix} H_0^{\ell m} Y_{\ell m} & H_1^{\ell m} Y_{\ell m} & h_0^{\ell m} \partial_\theta Y_{\ell m} & h_0^{\ell m} \partial_\phi Y_{\ell m} \\ \mathrm{Sym} & H_2^{\ell m} Y_{\ell m} & h_1^{\ell m} \partial_\theta Y_{\ell m} & h_1^{\ell m} \partial_\phi Y_{\ell m} \\ \mathrm{Sym} & \mathrm{Sym} & r^2 \left(K^{\ell m} + G^{\ell m} \partial_{\theta\theta}\right) Y_{\ell m} & r^2 G^{\ell m} \left(\partial_\theta - \cot\theta\right) \partial_\phi Y_{\ell m} \\ \mathrm{Sym} & \mathrm{Sym} & \mathrm{Sym} & r^2 \sin^2\theta \left[K^{\ell m} + G^{\ell m} \left(\cot\theta\, \partial_\theta + \sin^{-2}\theta\, \partial_{\phi\phi}\right)\right] Y_{\ell m} \end{pmatrix}. \quad (A3)$$

Here the spherical harmonics $Y_{\ell m}(\theta, \phi)$ form a complete orthonormal system and are eigenvectors of the operator $-\left[\partial_{\theta\theta} + \cot\theta \partial_\theta + \sin^{-2}\theta \partial_{\phi\phi}\right]$ with eigenvalue $\ell(\ell+1)$. A straightforward calculation shows that the following linear combinations of the perturbation functions are invariant under first-order coordinate transformations

$$q_1^{\ell m} = \frac{2\mathcal{M}r^2}{r - 2\mathcal{M}} \partial_t K^{\ell m} + r\frac{r - 3\mathcal{M}}{r - 2\mathcal{M}} K^{\ell m} - \frac{4\mathcal{M}^2}{r - 2\mathcal{M}} H_0^{\ell m}$$
$$+ r^2 \partial_r K^{\ell m} - (r - 2\mathcal{M}) H_2^{\ell m} - 4\mathcal{M} H_1^{\ell m},$$

$$q_2^{\ell m} = 2h_1^{\ell m} + \frac{4\mathcal{M}}{r - 2\mathcal{M}} h_0^{\ell m} - r^2 \partial_r G^{\ell m} - \frac{2\mathcal{M}r^2}{r - 2\mathcal{M}} \partial_t G^{\ell m}$$
$$- \frac{r^2}{r - 2\mathcal{M}} K^{\ell m}. \quad (A4)$$

The Zerilli function for arbitrary values of ℓ and m is given in terms of these variables by

$$\Psi_{\ell m} = \frac{-2(r - 2\mathcal{M})}{[\ell(\ell+1) - 2]r + 6\mathcal{M}} [2q_1^{\ell m} + \ell(\ell+1) q_2^{\ell m}], \quad (A5)$$

and represents the dynamical degree of freedom of the polar perturbations of the black hole. The evolution of the Zerilli function is determined by the perturbed Einstein field equations which can be written in the form

$$\left(1 + \frac{2\mathcal{M}}{r}\right)\partial_{tt}\Psi_{\ell m} - 4\frac{\mathcal{M}}{r}\partial_{tr}\Psi_{\ell m} - \left(1 - \frac{2\mathcal{M}}{r}\right)\partial_{rr}\Psi_{\ell m} + \frac{2\mathcal{M}}{r^2}(\partial_t\Psi_{\ell m} - \partial_r\Psi_{\ell m}) + V_\ell\Psi_{\ell m} = 0, \qquad \text{(A6)}$$

with the potential

$$V_\ell = \frac{\ell(\ell+1)[\ell(\ell+1)-2]^2r^3 + 6[\ell(\ell+1)-2]^2\mathcal{M}r^2 + 36[\ell(\ell+1)-2]\mathcal{M}^2r + 72\mathcal{M}^3}{r^3\{[\ell(\ell+1)-2]r+6\mathcal{M}\}^2}. \qquad \text{(A7)}$$

This is the well known Zerilli equation written in Kerr-Schild background coordinates. The more familiar form

$$\partial_{t_*t_*}\Psi_{\ell m} - \partial_{r_*r_*}\Psi_{\ell m} + \bar{V}_\ell\Psi_{\ell m} = 0 \qquad \text{(A8)}$$

using Schwarzschild time t_* and the tortoise coordinate r_* is directly obtained from the coordinate transformation

$$\begin{aligned} t_* &= t - 2\mathcal{M}\ln\frac{r-2\mathcal{M}}{D}, \\ r_* &= r + 2\mathcal{M}\ln\frac{r-2\mathcal{M}}{2\mathcal{M}}. \end{aligned} \qquad \text{(A9)}$$

Here D is an arbitrary constant of dimension length and $\bar{V}_\ell = (1 - 2\mathcal{M}/r)V_\ell$.

The derivation of the Zerilli function for given values of ℓ and m from a non-linear numerical simulation is performed as follows. We first calculate the physical 4-metric from the BSSN-variables and interpolate onto a sphere of constant extraction radius r_{ex}. Next we transform from Cartesian to spherical metric components. The key step is to use the orthogonality relations of the tensor harmonics which enable us to separate the contributions of the individual multipole moments from the metric. A straightforward albeit lengthy calculation shows that the perturbation functions are related to the spherical 4-metric components by

$$\begin{aligned} H_0^{\ell m} &= \int g_{tt}Y_{\ell m}^*d\Omega, \\ H_1^{\ell m} &= \int g_{tr}Y_{\ell m}^*d\Omega, \\ H_2^{\ell m} &= \int g_{rr}Y_{\ell m}^*d\Omega, \\ h_0^{\ell m} &= \frac{1}{\ell(\ell+1)}\int g_{t\theta}\,\partial_\theta Y_{\ell m}^* + \frac{g_{t\phi}}{\sin^2\theta}\,\partial_\phi Y_{\ell m}^*d\Omega \\ h_1^{\ell m} &= \frac{1}{\ell(\ell+1)}\int g_{r\theta}\,\partial_\theta Y_{\ell m}^* + \frac{g_{r\phi}}{\sin^2\theta}\,\partial_\phi Y_{\ell m}^*d\Omega \\ G^{\ell m} &= \frac{1}{r^2\,\ell(\ell+1)[\ell(\ell+1)-2]} \\ &\quad \int\left(g_{\theta\theta} - \frac{g_{\phi\phi}}{\sin^2\theta}\right)W_{\ell m}^* + 2\frac{g_{\theta\phi}}{\sin\theta}\frac{X_{\ell m}^*}{\sin\theta}d\Omega, \\ K^{\ell m} &= \frac{\ell(\ell+1)}{2}G^{\ell m} \\ &\quad + \frac{1}{2r^2}\int\left(g_{\theta\theta} + \frac{g_{\phi\phi}}{\sin^2\theta}\right)Y_{\ell m}^*d\Omega, \qquad \text{(A10)} \end{aligned}$$

where a superscript * denotes the complex conjugate,

$$X_{\ell m} = 2(\partial_\theta - \cot\theta)\partial_\phi Y_{\ell m} \qquad \text{(A11)}$$

$$W_{\ell m} = \left(\partial_{\theta\theta} - \cot\theta\partial_\theta - \frac{1}{\sin^2\theta}\partial_{\phi\phi}\right)Y_{\ell m}, \quad \text{(A12)}$$

and the integration is performed over the sphere of constant extraction radius. In order to also calculate the derivatives in Eq. (A4), we extract the perturbation functions at radii $r_{\text{ex}} - dr$, r_{ex} and $r_{\text{ex}} + dr$ on every time slice which contains the corresponding refinement level. The Zerilli function then follows directly from Eqs. (A4), (A5).

We have tested the wave extraction with the analytic solution of Teukolsky [60], which describes a quadrupole wave in linearized general relativity. The background is the Minkowski metric in this case which corresponds to the limit $\mathcal{M} = 0$ in the relations of this section. Because the quadrupole $\ell = 2$, $m = 0$ is the dominant multipole for all simulations discussed in this work, we also choose the Teukolsky wave with $m = 0$. In prescribing the free function F [cf. Eq. (6) in [60]], we follow the suggestion by Eppley [61] and superpose an ingoing and an outgoing
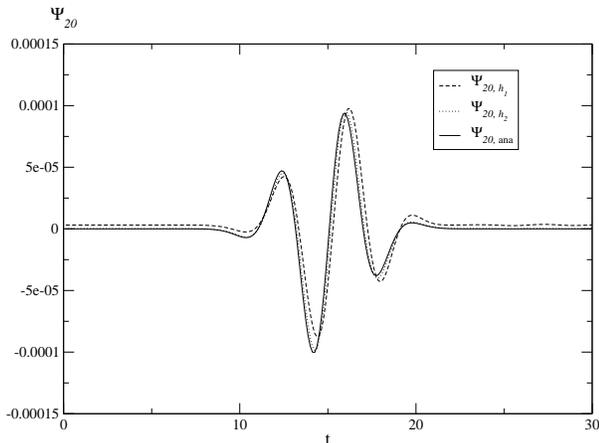
FIG. 9: The numerically calculated waveforms (dashed and dotted curve) for the $\ell = 2$, $m = 0$ Teukolsky wave are compared with the analytic result (solid curve).

wave packet. This packet is of Gaussian-like shape

$$F(x) = axe^{(-x/\sigma)^2}, \qquad (A13)$$

with $x = t \mp r$. The resulting analytic expression for the Zerilli function Ψ_{20} is rather lengthy but calculated straightforwardly. We evolve these data for $a = 10^{-5}$ and $\sigma = 1$ in octant symmetry on a numerical domain of size 20^3 with two refinement levels, the fine level having half the extent and twice the resolution of the coarse. In Fig. 9 we compare the numerically computed Ψ_{20} for resolutions $h_1 = 0.25$ (dashed) and $h_2 = 0.125$ (dotted curve) in the finer refinement level. We have also doubled the number of points on the extraction sphere from 80×40 to 160×80 in the θ and ϕ direction. In comparison the solid line represents the analytic result and demonstrates the convergence of the wave-forms. A quantitative evaluation shows that the convergence is fourth order in the early and late stages of this simulation and about third order in between when the wave pulse reaches the extraction radius $r_{\rm ex} = 15$. This behavior is compatible with the fact that we use a fourth-order integration scheme for the integration on the sphere and the main evolution code is second-order convergent.

[1] M. Shibata, K. Taniguchi, and K. Uryū, Phys. Rev. D **68**, 084020 (2003), gr-qc/0310030.
[2] P. Marronetti, M. D. Duez, S. L. Shapiro, and T. Baumgarte, Phys. Rev. Lett. **92**, 141101 (2004), gr-qc/0312036.
[3] B. Brügmann, W. Tichy, and N. Jansen, Phys. Rev. Lett. **92**, 211101 (2004), gr-qc/0312112.
[4] K. R. Eppley, Ph.D. thesis, Princeton University (1975).
[5] L. Smarr, A. Čadež, B. DeWitt, and K. Eppley, Phys. Rev. D **14**, 2443 (1976).
[6] L. Smarr, in *Sources of Gravitational Radiation*, edited by L. Smarr (Cambridge University Press, Cambridge, 1979), pp. 245–274.
[7] M. Shibata and T. Nakamura, Phys. Rev. D **52**, 5428 (1995).
[8] H. Friedrich, Class. Quantum Gravit. **13**, 1451 (1996).
[9] S. Frittelli and O. A. Reula, Phys. Rev. Lett. **76**, 4667 (1996), gr-qc/9605005.
[10] A. Anderson and J. W. York, Jr., Phys. Rev. Lett. **82**, 4384 (1999), gr-qc/9901021.
[11] T. W. Baumgarte and S. L. Shapiro, Phys. Rev. D **59**, 024007 (1999), gr-qc/9810065.
[12] M. Alcubierre, G. Allen, B. Brügmann, E. Seidel, and W.-M. Suen, Phys. Rev. D **62**, 124011 (2000), gr-qc/9908079.
[13] L. E. Kidder, M. A. Scheel, and S. A. Teukolsky, Phys. Rev. D **64**, 064017 (2001), gr-qc/0105031.
[14] G. Yoneda and H.-A. Shinkai, Phys. Rev. D **66**, 124003 (2002), gr-qc/0204002.
[15] O. Sarbach and M. Tiglio, Phys. Rev. D **66**, 064023 (2002), gr-qc/0205086.
[16] C. Bona, T. Ledvinka, C. Palenzuela, and M. Žáček, Phys. Rev. D **67**, 104005 (2003), gr-qc/0302083.

[17] M. Alcubierre and B. Brügmann, Phys. Rev. D **63**, 104006 (2001), gr-qc/0008067.
[18] H.-J. Yo, T. W. Baumgarte, and S. L. Shapiro, Phys. Rev. D **66**, 084026 (2002), gr-qc/0209066.
[19] M. Alcubierre, B. Brügmann, P. Diener, M. Koppitz, D. Pollney, E. Seidel, and R. Takahashi, Phys. Rev. D **67**, 084023 (2003), gr-qc/0206072.
[20] U. Sperhake, K. L. Smith, B. Kelly, P. Laguna, and D. Shoemaker, Phys. Rev. D **69**, 024012 (2004), gr-qc/0307015.
[21] S. Brandt, R. Correll, R. Gómez, M. Huq, P. Laguna, L. Lehner, P. Maronetti, R. A. Matzner, D. Neilsen, J. Pullin, et al., Phys. Rev. Lett. **85**, 5496 (2000), gr-qc/0009047.
[22] M. Alcubierre, B. Brügmann, P. Diener, F. Herrmann, D. Pollney, E. Seidel, and R. Takahashi (2004), gr-qc/0411137.
[23] M. Alcubierre, B. Brügmann, P. Diener, F. S. Guzmán, I. Hawke, S. Hawley, F. Herrmann, M. Koppitz, D. Pollney, E. Seidel, et al. (2004), AEI-2004-115, gr-qc/0411149.
[24] P. Anninos, D. Hobill, E. Seidel, L. Smarr, and W.-M. Suen, Phys. Rev. Lett. **71**, 2851 (1993), gr-qc/9309016.
[25] P. Anninos, D. Hobill, E. Seidel, L. Smarr, and W.-M. Suen, Phys. Rev. D **52**, 2044 (1995).
[26] P. Anninos, R. H. Price, J. Pullin, E. Seidel, and W.-M. Suen, Phys. Rev. D **52**, 4462 (1995), gr-qc/9505042.
[27] J. Baker, A. Abrahams, P. Anninos, S. Brandt, R. Price, J. Pullin, and E. Seidel, Phys. Rev. D **55**, 829 (1997), gr-qc/9608064.
[28] P. Anninos and S. Brandt, Phys. Rev. Lett. **81**, 508 (1998), gr-qc/9806031.

[29] R. H. Price and J. Pullin, Phys. Rev. Lett. **72**, 3297 (1994), gr-qc/9402039.

[30] A. M. Abrahams and G. B. Cook, Phys. Rev. D **50**, R2364 (1994), gr-qc/9405051.

[31] R. J. Gleiser, C. O. Nicasio, R. H. Price, and J. Pullin, Phys. Rev. Lett. **77**, 4483 (1996), gr-qc/9609022.

[32] L. E. Simone, E. Poisson, and C. M. Will, Phys. Rev. D **52**, 4481 (1995), gr-qc/9506080.

[33] J. Baker, B. Brügmann, and M. Campanelli, Class. Quantum Grav. **17**, L149 (2000), gr-qc/0003027.

[34] B. Brügmann, Int. J. Mod. Phys. **8**, 85 (1999), gr-qc/9708035.

[35] M. Alcubierre, W. Benger, B. Bügmann, G. Lanfermann, and L. Nerger, Phys. Rev. Lett. **87**, 271103 (2001), gr-qc/0012079.

[36] D. Shoemaker, K. Smith, U. Sperhake, P. Laguna, E. Schnetter, and D. Fiske, Class. Quantum Grav. **20**, 3729 (2003), gr-qc/0301111.

[37] E. Schnetter, S. H. Hawley, and I. Hawke, Class. Quant. Grav. **21**, 1465 (2004), gr-qc/0310042.

[38] G. B. Cook, Living Rev. Relativity **2000-5** (2000), [Online Article] cited on 30 Sep 2004, http://relativity.livingreviews.org/Articles/lrr-2000-5.

[39] R. A. Matzner, M. F. Huq, and D. Shoemaker, Phys. Rev. D **59**, 024015 (1998), gr-qc/9805023.

[40] P. Marronetti, M. Huq, P. Laguna, L. Lehner, R. Matzner, and D. Shoemaker, Phys. Rev. D **62**, 024017 (2000), gr-qc/0001077.

[41] E. Bonning, P. Marronetti, D. Neilsen, and R. A. Matzner, Phys. Rev. D **68**, 044019 (2003), gr-qc/0305071.

[42] J. W. York, Jr., in *Sources of Gravitational Radiation*, edited by L. Smarr (Cambridge University Press, Cambridge, 1979), pp. 83–126.

[43] C. Bona, J. Massó, E. Seidel, and J. Stela, Phys. Rev. Lett. **75**, 600 (1995), gr-qc/9412071.

[44] M. Alcubierre, B. Brügmann, D. Pollney, E. Seidel, and R. Takanashi, Phys. Rev. D **64**, 061501 (2001), AEI-2001-021, gr-qc/0104020.

[45] M. Alcubierre, A. Corichi, J. A. Gonzáles, D. Núñez, and M. Salgado (2003), gr-qc/0303086.

[46] M. Alcubierre, A. Corichi, J. González, D. Núñez, and M. Salgado, Class. Quantum Grav. **20**, 3951 (2003), gr-qc/0303069.

[47] C. Gundlach and J. M. Martín-García, Phys. Rev. D **70**, 044032 (2004), gr-qc/0403019.

[48] T. W. Baumgarte, Phys. Rev. D **62**, 024018 (2000), gr-qc/0004050.

[49] G. B. Cook, Phys. Rev. D **50**, 5025 (1994), gr-qc/9404043.

[50] J. Thornburg, Phys. Rev. D **54**, 4899 (1996), gr-qc/9508014.

[51] J. Thornburg, Class. Quantum Grav. **21**, 743 (2004), gr-qc/0306056.

[52] L. Gunnarsen, H.-A. Shinkai, and K.-I. Maeda, Class. Quant. Grav. **12**, 133 (1995), gr-qc/9406003.

[53] W. Kinnersley, J. Math. Phys. **10**, 1195 (1969).

[54] S. Chandrasekhar and S. Detweiler, Proc. R. Soc. Lond. A. **344**, 441 (1975).

[55] C. T. Cunningham, R. H. Price, and V. Moncrief, ApJ **236**, 674 (1980).

[56] V. Moncrief, Ann. Phys. **88**, 323 (1974).

[57] A. M. Abrahams and C. R. Evans, Phys. Rev. D **42**, 2585 (1990).

[58] A. Abrahams, D. Bernstein, D. Hobill, E. Seidel, and L. Smarr, Phys. Rev. D **45**, 3544 (1992).

[59] T. Regge and J. A. Wheeler, Phys. Rev. **108**, 1063 (1957).

[60] S. A. Teukolsky, Phys. Rev. D **26**, 745 (1982).

[61] K. Eppley, in *Sources of Gravitational Radiation*, edited by L. L. Smarr (Cambridge University Press, Cambridge, 1979), pp. 275–291.